The Astrophysical Journal, 833:32 (10pp), 2016 December 10 doi:10.3847/1538-4357/833/1/32

POLARIZED LINE FORMATION IN NON-MONOTONIC VELOCITY FIELDS

M. Sampoorna and K. N. Nagendra
Indian Institute of Astrophysics, Koramangala, Bengaluru 560034, India; sampoorna@iiap.res.in, knn@iiap.res.in
Received 2016 February 18; revised 2016 October 7; accepted 2016 October 11; published 2016 December 6

ABSTRACT

For a correct interpretation of the observed spectro-polarimetric data from astrophysical objects such as the Sun, it is necessary to solve the polarized line transfer problems taking into account a realistic temperature structure, the dynamical state of the atmosphere, a realistic scattering mechanism (namely, the partial frequency redistribution—PRD), and the magnetic fields. In a recent paper, we studied the effects of monotonic vertical velocity fields on linearly polarized line profiles formed in isothermal atmospheres with and without magnetic fields. However, in general the velocity fields that prevail in dynamical atmospheres of astrophysical objects are non-monotonic. Stellar atmospheres with shocks, multi-component supernova atmospheres, and various kinds of wave motions in solar and stellar atmospheres are examples of non-monotonic velocity fields. Here we present studies on the effect of non-relativistic non-monotonic vertical velocity fields on the linearly polarized line profiles formed in semi-empirical atmospheres. We consider a two-level atom model and PRD scattering mechanism. We solve the polarized transfer equation in the comoving frame (CMF) of the fluid using a polarized accelerated lambda iteration method that has been appropriately modified for the problem at hand. We present numerical tests to validate the CMF method and also discuss the accuracy and numerical instabilities associated with it.

Key words: line: profiles – polarization – radiative transfer – scattering – stars: atmospheres – Sun: chromosphere

1. INTRODUCTION

High-resolution observations of the outer layers of the Sun (namely, the chromosphere and transition region) show that these layers are not quiet and homogeneous but dynamic, and appear to change constantly on all observable scales (see e.g., Rutten 2007). Analysis of such a complex environment requires detailed radiative transfer computations in dynamical atmospheres especially for optically thick lines. The linear polarization of radiation (which is produced by resonance scattering processes in these layers) is significantly affected by the dynamical nature of the solar (and in general stellar) atmospheres (see e.g., Carlin et al. 2013; Carlin & Asensio Ramos 2015).

In Sampoorna & Nagendra (2015a, 2015b) we studied the effects of monotonic vertical velocity fields on the linear polarization profiles formed in isothermal one-dimensional atmospheres. The governing equations and the numerical method of solution for solving the concerned problem of polarized radiative transfer in the presence of a vertical monotonic velocity field are presented in Sampoorna & Nagendra (2015b, hereafter P1). There, we presented both the observer's frame and comoving frame (CMF) methods, which are based on the concept of operator perturbation (see Cannon 1973). More specifically we extended the CMF method of Hauschildt & Baron (2004) to include polarization and partial frequency redistribution (PRD).[1] We remark that, unlike Hauschildt & Baron (2004), who consider a fully relativistic CMF transfer equation in a spherical geometry, we consider (i) a planar geometry and (ii) the CMF transfer equation in the limit whereby only Doppler shifts are taken into account (see Mihalas 1978). Thus P1 and the present paper can handle only non-relativistic vertical velocity fields. The advantages of the CMF method over the observer's frame method are well known for the case of unpolarized radiative transfer (see e.g., Noerdlinger & Rybicki 1974; Mihalas 1978; Hubeny & Mihalas 2014, and the references cited therein). In particular the CMF is the method of choice when (i) PRD in line scattering is taken into account and/or (ii) when the maximum Doppler shift in the plasma is much larger than the Doppler width, which however does not prevail in the solar atmosphere. The advantages of using the CMF method turn out to be even greater when polarization and magnetic fields are included in the current problem. This is because the PRD function required for the unpolarized case has to be replaced by a PRD matrix that requires larger memory and is also computationally expensive (see the Appendix in P1).

In the present paper we suitably modify the CMF method presented in P1 to include non-monotonic vertical velocity fields. To this end we again follow the CMF method of Hauschildt & Baron (2004). The CMF transfer equation is a partial integro-differential equation involving both spatial and frequency derivatives. Thus this equation represents an initio-boundary value problem. In the case of planar geometry the choice of the initial condition in frequency is unique and depends only on the sign of the velocity gradient (see Mihalas et al. 1976; Mihalas 1978), irrespective of the nature of the velocity field. This is not the case for spherical geometry (see Appendix A of Mihalas et al. 1975). Thus the CMF method of P1 can be applied to handle non-monotonic velocity fields with small modifications that are detailed in Section 2 below.

For a planar geometry, the CMF method using a Feautrier-type elimination scheme was developed by Noerdlinger & Rybicki (1974) and Mihalas et al. (1976) for solving respectively unpolarized line transfer with complete frequency redistribution (CRD) and the type-I angle-averaged PRD function of Hummer (1962). Their methods could handle both monotonic and non-monotonic velocity fields. For a spherical geometry, the CMF methods for solving the unpolarized line transfer have been developed by several workers in the field. We refer only to those papers whose methods of solution have

[1] In P1, as an oversight it is mentioned that we extended the CMF method of Baron & Hauschildt (2004) to include polarization and PRD; instead it should be the second discretization scheme of Hauschildt & Baron (2004).

been suitably adopted in P1 and the present paper. A CMF method based on operator perturbation was developed by Hauschildt (1992) to solve the fully relativistic, spherically symmetric unpolarized radiative transfer equation in the CMF including monotonic velocity fields. The discretization scheme used by Hauschildt (1992), referred to as a first discretization scheme by Hauschildt & Baron (2004) for the frequency derivative term of the CMF transfer equation, although fully implicit, was somewhat less accurate and did not allow one to include the effects of the frequency derivative in the construction of the approximate lambda operator used in the operator splitting method. These difficulties were overcome by Hauschildt & Baron (2004) who introduced a second discretization scheme which led to significantly less numerical diffusion than the earlier scheme of Hauschildt (1992). The CMF method presented in P1 is actually based on this second discretization of Hauschildt & Baron (2004). In Baron & Hauschildt (2004), the second discretization was further generalized to handle non-monotonic velocity fields.

The effects of vertical velocity fields on the linear polarization profiles are presented in detail in Carlin et al. (2012, 2013) for the case of CRD and in Nagendra (1996) and Sampoorna & Nagendra (2015a, 2015b) for the case of PRD. However it is important to note that the basic effects of the vertical velocity fields on linear polarization depend on the relation between the angular-dependent Doppler shifts and the radiation field anisotropy, and not on the type of frequency redistribution used. It is well known that PRD effects are generally significant mainly in the line wings than in the line core. For a chromospheric line (such as the Ca I 4227 Å resonance line), the PRD wings are mainly formed in the sub-chromospheric layers (see e.g., Faurobert-Scholl 1992; Holzreuter et al. 2005). In the real solar atmosphere, the velocities are generally significantly reduced in those layers where PRD wings are formed. Therefore the effects of velocity may not be crucial when considering linear polarization in the PRD wings. However, if under certain conditions a spatially confined shock-like transition in velocity gradient occurs in these sub-chromospheric layers, then such velocities will certainly have an effect on the linear polarization of the PRD wings. Thus here we study the effects of non-monotonic vertical velocity fields on the linearly polarized line profiles that are governed by PRD, although the velocity field and the model atmosphere chosen are far from realistic.

Traditionally, the solar atmosphere has been represented through one-dimensional hydrostatic models which include a sophisticated radiative transfer treatment (see e.g., Vernazza et al. 1981; Fontenla et al. 1993, 2009). These models have been quite successfully used to reproduce the spatially and temporally averaged observed linearly polarized spectra of several important spectral lines formed in the solar atmosphere (see e.g., Anusha et al. 2010, 2011; Supriya et al. 2014; Smitha et al. 2015). Therefore these models can be assumed to reasonably represent the average properties of the solar atmosphere. In this paper we assume a plane-parallel one-dimensional atmosphere with a temperature structure given by the model-C (hereafter VALC) of Vernazza et al. (1981). Assuming the temperature structure to be unaffected by the velocity field, we consider time-dependent or time-independent non-monotonic vertical velocity fields.

The paper is organized as follows. In Section 2 we briefly recall the basic equations and present the necessary modifications made in the formal solution to handle the non-monotonicity of the velocity field. The atomic and atmospheric models, and the different types of velocity fields used in our computations, are discussed respectively in Sections 3 and 4. Numerical validation of the CMF methods presented in P1 and in this paper is discussed in Section 5. The linear polarization profiles formed in the VALC model atmosphere are presented in Section 6 for the non-magnetic case. Our conclusions are presented in Section 7.

2. STATEMENT OF THE PROBLEM AND PROCEDURE FOR ITS SOLUTION

We consider a one-dimensional planar atmosphere with velocity fields along the atmospheric normal, and a two-level atom model with infinitely sharp and unpolarized lower level. For computational simplicity, we consider only the case of angle-averaged PRD. Further, we recall only those equations which are necessary to incorporate non-monotonic nature of the velocity field. In the presence of a weak magnetic field the polarized radiation field is represented by the three-component Stokes vector $\boldsymbol{I} = (I, Q, U)^{\mathrm{T}}$, which is in general non-axisymmetric. The positive Q direction is defined to be perpendicular to the nearest limb. It is possible to decompose this non-axisymmetric Stokes vector into six irreducible components that are cylindrically symmetric (Frisch 2007). From here on we present all the basic equations in this irreducible basis (see P1 for more details).

The CMF transfer equation for unpolarized intensity in planar atmospheres and for non-relativistic velocity fields is given in Equation (14.99) of Mihalas (1978). When polarization and magnetic fields are taken into account the CMF transfer equation takes the form:

$$\frac{\partial \boldsymbol{\mathcal{I}}(\tau, x, \mu)}{\partial \tau} = \boldsymbol{\mathcal{I}}(\tau, x, \mu) - \boldsymbol{\mathcal{S}}(\tau, x) - \tilde{\boldsymbol{\mathcal{S}}}(\tau, x, \mu), \qquad (1)$$

where $\boldsymbol{\mathcal{I}}$ is a six-component, cylindrically symmetric intensity vector and $\mu = \cos\theta$ with θ the co-latitude. The monochromatic optical depth along the ray is given by $d\tau = [\varphi(x) + r]d\tau_l/\mu$, where $d\tau_l$ is the line integrated optical depth and r denotes the ratio of the continuum to the line-integrated absorption coefficient. The absorption profile function is $\varphi(x) = H(a, x)$, where a is the damping parameter and $x = (\nu - \nu_0)/\Delta\nu_{\mathrm{D}}$ (with ν_0 being the line center frequency and $\Delta\nu_{\mathrm{D}}$ the Doppler width). The CMF term $\tilde{\boldsymbol{\mathcal{S}}}(\tau, x, \mu)$ is given by

$$\tilde{\boldsymbol{\mathcal{S}}}(\tau, x, \mu) = -\mu\left[\frac{\mu}{\varphi(x) + r}\,\frac{1}{v_{\mathrm{th}}}\,\frac{dv_z}{d\tau_l}\right]\frac{\partial \boldsymbol{\mathcal{I}}(\tau, x, \mu)}{\partial x}, \qquad (2)$$

where v_z is the vertical velocity field and v_{th} is the thermal velocity. For an isothermal atmosphere v_{th} is a constant. We now define the non-dimensional velocity $V = v_z/v_{\mathrm{th}}$. Thus the term in the square brackets of Equation (2) simplifies to $dV/d\tau$ as in Equation (14) of P1. For an atmosphere with temperature gradient, v_{th} (as well as $\Delta\nu_{\mathrm{D}}$) will vary with depth, and therefore we retain this term as it is in Equation (2). The total source vector is given by

$$\boldsymbol{\mathcal{S}}(\tau, x) = \frac{\varphi(x)\boldsymbol{\mathcal{S}}_l(\tau, x) + r\boldsymbol{\mathcal{S}}_c}{\varphi(x) + r}, \qquad (3)$$

Table 1
The Values of Coefficients p at Any Spatial Point O

	$\left(\frac{dv_z}{d\tau_l}\right)_O \geqslant 0$	$\left(\frac{dv_z}{d\tau_l}\right)_O < 0$
$p^O_{m,m-1}$	$-\frac{1}{x_m - x_{m-1}}$	0
$p^O_{m,m}$	$\frac{1}{x_m - x_{m-1}}$	$\frac{1}{x_m - x_{m+1}}$
$p^O_{m,m+1}$	0	$-\frac{1}{x_m - x_{m+1}}$

where the continuum source vector $\boldsymbol{\mathcal{S}}_c = B_{\nu_0}\boldsymbol{\mathcal{U}}$, with B_{ν_0} the Planck function at the line center and $\boldsymbol{\mathcal{U}} = (1, 0, 0, 0, 0, 0)^T$ and the line source vector has the form

$$\boldsymbol{\mathcal{S}}_l(\tau, x) = \boldsymbol{\mathcal{G}}(\tau) + \int_{-\infty}^{+\infty} dx' \frac{1}{2}\int_{-1}^{+1} d\mu' \times \frac{\boldsymbol{N}^r(x, x', \boldsymbol{B})}{\varphi(x)}\,\boldsymbol{\Psi}(\mu')\boldsymbol{\mathcal{I}}(\tau, x', \mu'). \quad (4)$$

Here $\boldsymbol{\mathcal{G}}(\tau) = \epsilon B_{\nu_0}\boldsymbol{\mathcal{U}}$ is the primary source vector, with ϵ being the thermalization parameter. The explicit form of the 6×6 Hanle PRD matrix $\boldsymbol{N}^r(x, x', \boldsymbol{B})$ and of the 6×6 Rayleigh phase matrix $\boldsymbol{\Psi}(\mu)$ are respectively given in Appendix A of Sampoorna et al. (2008) and Frisch (2007).

We determine the formal solution of Equation (1) using the short-characteristic method of Olson & Kunasz (1987). As done in Hauschildt & Baron (2004, and also in P1), we use parabolic interpolation (with coefficients Ψ_M, Ψ_O, and Ψ_P) for $\boldsymbol{\mathcal{S}}$ and linear interpolation (with coefficients Ψ'_M and Ψ'_O) for the CMF term $\tilde{\boldsymbol{\mathcal{S}}}$. Thus at any spatial point "O" and frequency point (say x_m) the polarized radiation field $\boldsymbol{\mathcal{I}}$ is given by

$$\begin{aligned}\boldsymbol{\mathcal{I}}_O(x_m, \mu) = {} & e^{-\Delta\tau_{MO}}\boldsymbol{\mathcal{I}}_M(x_m, \mu) \\ & + \Psi_M\boldsymbol{\mathcal{S}}_M(x_m) + \Psi_O\boldsymbol{\mathcal{S}}_O(x_m) + \Psi_P\boldsymbol{\mathcal{S}}_P(x_m) \\ & + \Psi'_M\,\tilde{\boldsymbol{\mathcal{S}}}_M(x_m, \mu) + \Psi'_O\,\tilde{\boldsymbol{\mathcal{S}}}_O(x_m, \mu), \end{aligned} \quad (5)$$

where M and P are the upwind and downwind points respectively, and $\Delta\tau_{MO}$ is the optical distance on the segment MO. We remark that the CMF terms $\tilde{\boldsymbol{\mathcal{S}}}_M$ and $\tilde{\boldsymbol{\mathcal{S}}}_O$ depend on the monotonicity of the velocity field and on the kind of frequency derivative scheme used for evaluating Equation (2).

The CMF transfer equation (Equation (1)) represents an initial plus boundary value problem, wherein the initial condition is uniquely defined for a planar geometry. For a given depth point the initial condition in frequency depends only on the sign of the velocity gradient and is independent of the nature of the velocity field. Therefore the frequency discretization scheme used in P1 (see their Equation (20)) can also be applied to the present case of non-monotonic vertical velocity fields. However to clearly reflect the change in the sign of velocity gradient from one depth point to the other (occurring due to the non-monotonic nature of the velocity field) in the expressions for $\tilde{\boldsymbol{\mathcal{S}}}_M$ and $\tilde{\boldsymbol{\mathcal{S}}}_O$, we define

$$\begin{aligned}\left(\frac{\partial\boldsymbol{\mathcal{I}}}{\partial x}\right)_{O,x_m} = {} & p^O_{m,m-1}\boldsymbol{\mathcal{I}}_O(x_{m-1}, \mu) \\ & + p^O_{m,m}\boldsymbol{\mathcal{I}}_O(x_m, \mu) + p^O_{m,m+1}\boldsymbol{\mathcal{I}}_O(x_{m+1}, \mu), \end{aligned} \quad (6)$$

where the coefficients p are listed in Table 1. We remark that the frequency discretization scheme defined in Equation (6) is the same as that defined in Hauschildt & Baron (2004) and Baron & Hauschildt (2004), namely a local upwind scheme. Thus for a given depth point one of the coefficients p is always zero and the other two take different values depending on the sign of the velocity gradient (see Table 1).

For $(dv_z/d\tau_l)_O \geqslant 0$, we impose the initial condition[2] $(\partial\boldsymbol{\mathcal{I}}/\partial x)_O = 0$ at $x = -x_{max}$. In other words all the coefficients p are set to zero at $x = -x_{max}$ and the frequency integration proceeds from $-x_{max}$ to $+x_{max}$. In contrast, for $(dv_z/d\tau_l)_O < 0$ all the coefficients p are set to zero at $x = +x_{max}$ and the frequency integration proceeds from $+x_{max}$ to $-x_{max}$. Clearly the initial condition $\partial\boldsymbol{\mathcal{I}}/\partial x = 0$ is applied at all the depth points in the planar atmosphere, either at $x = +x_{max}$ or at $x = -x_{max}$ depending on the sign of the velocity gradient. It is important to note that the initial condition $\partial\boldsymbol{\mathcal{I}}/\partial x = 0$ should be applied at a very far-wing frequency wherein the intensity and polarization have indeed become flat. Otherwise numerical oscillations in the far-wing solution would occur (see Nagendra 1996 for a discussion of this point). For the isothermal model atmosphere considered in P1, the initial condition at all depth points was imposed at $|x_{max}| = 4000$ Doppler widths and for the VALC model atmosphere considered in this paper it is imposed at $|x_{max}| \approx 200$ Doppler widths (i.e., at 10 Å from the line center). We have verified that at these frequencies the intensity and polarization reach the continuum value and are nearly flat.

Substituting Equation (6) in (2) and the resulting expression in Equation (5), we obtain the short-characteristic formal solution in a CMF as

$$\begin{aligned}&\left[1 + \Psi'_O\mu\left(\frac{\mu}{\varphi(x_m) + r}\frac{1}{v_{th}}\frac{dv_z}{d\tau_l}\right)_O p^O_{m,m}\right]\boldsymbol{\mathcal{I}}_O(x_m, \mu) \\ &= e^{-\Delta\tau_{MO}}\boldsymbol{\mathcal{I}}_M(x_m, \mu) \\ &\quad + \Psi_M\boldsymbol{\mathcal{S}}_M(x_m) + \Psi_O\boldsymbol{\mathcal{S}}_O(x_m) + \Psi_P\boldsymbol{\mathcal{S}}_P(x_m) \\ &\quad + \Psi'_M\,\tilde{\boldsymbol{\mathcal{S}}}_M(x_m, \mu) - \Psi'_O\,\mu\left(\frac{\mu}{\varphi(x_m) + r}\frac{1}{v_{th}}\frac{dv_z}{d\tau_l}\right)_O \\ &\quad \times [p^O_{m,m-1}\boldsymbol{\mathcal{I}}_O(x_{m-1}, \mu) + p^O_{m,m+1}\boldsymbol{\mathcal{I}}_O(x_{m+1}, \mu)]. \end{aligned} \quad (7)$$

We remark that, when computing the $\tilde{\boldsymbol{\mathcal{S}}}_M(x_m, \mu)$, care should be taken to use the appropriate coefficients p based on the sign of $(dv_z/d\tau_l)_M$. When the velocity field has a known analytical form its gradient $dv_z/d\tau_l$ can also be computed analytically. For an arbitrary velocity field, the gradient can be computed using a highly accurate cubic spline interpolation subroutine.

3. THE ATOMIC AND ATMOSPHERIC MODELS

We consider a two-level atom model with lower and upper level total angular momentum quantum numbers 0 and 1 respectively. In particular, we consider a resonance line with a line center wavelength at 4226.7 Å which is representative of the well-known Ca I 4227 Å line. The radiative width corresponding to this line is $\Gamma_R = 2.18 \times 10^8\ s^{-1}$. The Doppler width is given by

$$\Delta\nu_D = \frac{\nu_0}{c}\sqrt{\frac{2k_BT}{M_a} + v^2_{turb}}, \quad (8)$$

[2] For isothermal atmospheres the initial condition is imposed based on the sign of $dV/d\tau_l$ at each depth point. Therefore, in P1, below Equation (20), $dV/d\tau$ should read as $dV/d\tau_l$.

where c is the speed of light, k_B is the Boltzmann constant, and M_a is the mass of the Ca I atom. A constant micro-turbulent velocity $v_{\rm turb} = 2$ km s^{-1} is assumed.

We consider a depth-varying planar atmosphere given by the VALC model (Vernazza et al. 1981). Clearly, the non-dimensional frequency grid x and the damping parameter $a = \Gamma_R/(4\pi\Delta\nu_D)$ are depth dependent in our calculations. The other atmospheric parameters, namely, r and ϵ, are assumed to be constant and given by 10^{-5} and 10^{-4} respectively. The depolarizing elastic collisions are neglected.

We use a trapezoidal height grid with a spacing of $\Delta z = 15$ km, which corresponds to approximately 20 points per decade in the τ_l-scale. For the wavelength grid, namely $(\lambda - \lambda_0)$, we have about 141 points in the range -10 Å to $+10$ Å. In the range -0.4 Å to $+0.4$ Å, the grid is equally spaced with a spacing of 0.01 Å. Outside this range the wavelength grid is unequally spaced. For the angle grid, we use a seven-point Gauss–Legendre quadrature in the range $[0 < \mu \leqslant 1]$. The above-mentioned grid specifications are used for most of the figures presented in this paper, unless specified otherwise.

4. THE MODELS OF THE VELOCITY FIELDS

We consider two types of non-monotonic velocity fields. One represents a vertical velocity wave in the atmosphere. The other is the same as presented in Figure 6 of Carlin et al. (2012), namely, a positive monotonic velocity field v_z increasing linearly with different constant gradient (v_g) from the lower spatial boundary. We refer to this type of velocity field as the linear velocity field. In this case, the non-dimensional velocity V $(=v_z/v_{\rm th})$ is non-monotonic purely due to the depth dependence of the mean thermal velocity through temperature.

To represent the wave motion, we consider a propagating damped sine wave. Although such a representation of the wave motion is too crude to allow any detailed modeling, it however serves to illustrate some interesting effects in the time evolution of the linearly polarized line profiles. The effect of such a velocity wave on linearly polarized line profiles under the limit of CRD was studied by Rangarajan (1997, 1999, and references therein). Here we consider the case of line profiles formed under PRD.

In a dynamical solar atmosphere, acoustic and magneto-acoustic (Alfvén) waves are commonly found. These are topics of great interest as they are partly responsible for explaining the well-known problem of coronal heating (Parker 2007; Taroyan & Erdélyi 2009). Therefore it is necessary to understand the details of propagation of these waves in the entire solar atmosphere. To simulate a damped adiabatic acoustic wave, Scharmer (1984) proposed a vertical velocity field represented by a damped sine wave:

$$V = \frac{V_0}{1 + \sqrt{\tau_c/\tau^*}} \sin\left[\frac{2\pi\,(z - c_p t)}{c_p P}\right], \qquad (9)$$

where τ_c is the continuum optical depth, τ^* is the depth at which the amplitude of the wave saturates to V_0, z is the vertical height in the atmosphere, t is the time measured from initial time point $t = 0$ s, c_p is the propagation speed of the wave, and P is its period. For an exponentially stratified atmosphere $\tau_c = 2.2\exp(-z/H)$ with scale height $H = 120$ km. For all our computations, we have chosen $V_0 = -3$ Doppler units, $P = 100$ s, $c_p = 7$ km s^{-1}, and $\tau^* = 10^{-3}$. We remark that the velocity gradient can be determined by analytically differentiating Equation (9).

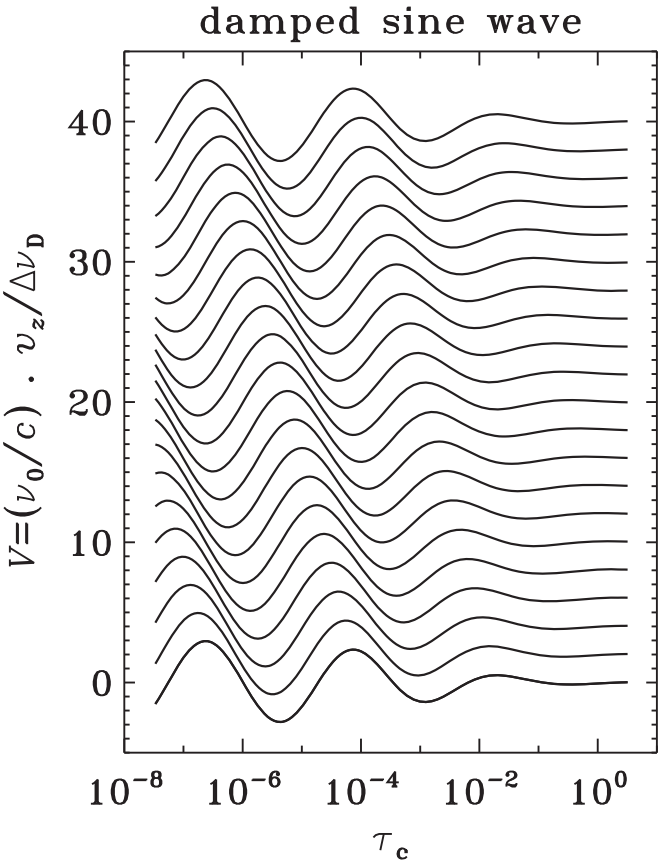

Figure 1. A vertical damped sine wave as a function of continuum optical depth τ_c in a VALC model atmosphere. From bottom to top, different curves show the velocity wave from 0 to 100 s in steps of 5 s. In order to clearly illustrate the time evolution, a constant upward shift is given to curves at different time points. Thus the ordinate values for only the bottom-most curve can be read. The amplitude (V_0) of the wave is -3 Doppler units, the period (P) is 100 s, the propagation speed (c_p) is 7 km s^{-1}, and $\tau^* = 10^{-3}$.

Figure 1 shows the variation of the vertical velocity wave given by Equation (9) with continuum optical depth for different time points. The velocity field variation is given for every five seconds, covering one full wave period.

5. NUMERICAL VALIDATION

In this section we discuss the numerical tests performed to validate the CMF methods presented in P1 and the present paper.

5.1. Comparison of Emergent Profiles Computed Using Comoving and Observer's Frame Methods

The CMF method can be validated by comparing the resulting emergent Stokes profiles with those from the observer's frame method. Such a comparison is presented in Figure 2 for a linear velocity field with $v_g = 20.07$ m s^{-1} km^{-1} (panel (a)) and for a damped sine wave at $t = 10$ s (panel (b)). The dotted curve represents the emergent solution from the observer's frame method and the dashed curve represents the CMF method. Clearly, the profiles from both methods coincide

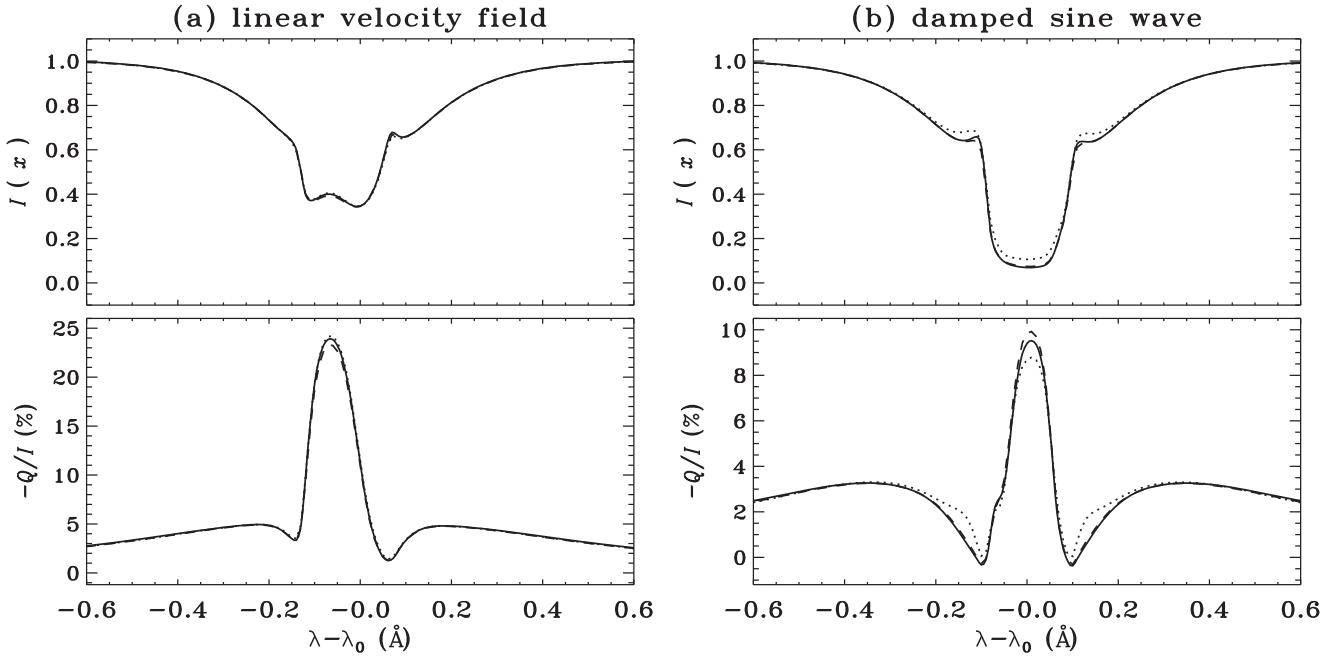

Figure 2. Comparison of emergent (I, Q/I) profiles at $\mu = 0.13$ computed using the observer's frame (dotted curves) and CMF (solid and dashed curves) methods. The VALC model atmosphere is used for the computation. Panel (a) corresponds to the case of a linear velocity field having a constant velocity gradient $v_g = 20.07\ \mathrm{m\ s^{-1}\ km^{-1}}$, and panel (b) to the case of a damped sine wave at $t = 10$ s (see Figure 1).

in the case of a linear velocity field. Small differences are seen around the line core region in the case of a damped sine wave (see panel (b)). These differences can be understood by considering that the emergent profiles from the CMF and observer's frame methods are computed using the spatial, wavelength, and angular grids specified in Section 3. Although these grids are sufficient for the CMF method (compare the solid and dashed curves), they are not precise enough for the observer's frame method. This is because in the latter method the inextricable coupling between spatial, wavelength, and angular points brought about by the velocity field places a severe demand on these grids (see e.g., Mihalas 1978). Obtaining an "exact solution" from the observer's frame method using very fine grids in all three variables is beyond the scope of the available computational facilities (see e.g., Table 1 in P1). Therefore we compute such a solution using the CMF method. The solid curve in Figure 2 is computed using this method with a 40 point per decade spatial grid, 281 point wavelength grid, and 35 point angular grid. Clearly, the solid and dashed curves for both velocity fields nearly coincide, thereby validating the accuracy of the solution obtained on a lower-resolution grid from the CMF method.

5.2. Numerical Accuracy of the CMF Method

Numerical accuracy of a converged numerical solution on a given grid is determined by the truncation error or the relative true error T_e (Auer et al. 1994). In Figure 3 we show the variation of relative true error corresponding to the $\mathcal{S}_0^0$ and $\mathcal{S}_0^2$ with the iteration number at the surface grid point for the CMF method. We recall that in the non-magnetic case the source vector $\boldsymbol{\mathcal{S}}$ comprises two non-zero components, namely $\mathcal{S}_0^0$ and $\mathcal{S}_0^2$.

To compute the true error on a spatial grid of 20 points per decade, a wavelength grid of 141 points, and 7 point angular grid, we compute the true solution on a 40 point per decade spatial grid, 281 point wavelength grid, and 35 point angular grid. For linear velocity fields, the surface true error of both source vector components are smaller than or comparable to the corresponding static case. For the case of a damped sine wave, the true error of $\mathcal{S}_0^0$ is nearly the same as the static case, while that of $\mathcal{S}_0^2$ is larger than the static case. This slightly larger true error can be attributed to the non-monotonic nature of the damped sine wave, which is perhaps not well represented by the local upwind scheme used for the frequency derivative term.

5.3. Numerical Instability of the CMF Method

Our numerical tests with very large velocity gradients, which give rise to maximum non-dimensional velocity V larger than 1000 Doppler widths within the atmosphere, show that the CMF methods presented in P1 and this paper become numerically unstable. This is particularly true for the strong line case considered in this paper, namely $r = 10^{-5}$. We remark that the CMF code does converge (in fact within 20–30 iterations) for such large velocity gradients, but the converged solution shows numerical oscillations. This is illustrated in Figure 4 for a strong line with $r = 10^{-5}$ (panels (a) and (b)) and for a weaker line with $r = 10^{-2}$ (panel (c)). A linear velocity field with $v_g = 1600\ \mathrm{m\ s^{-1}\ km^{-1}}$ is considered. For such high-velocity fields, both the strong and weaker lines are in emission due to extreme Doppler brightening.

For this study, we consider four types of wavelength grids with different spectral resolution within the range $[-100, +100]$ Å, so that the non-dimensional frequency x grid extends to about 10,000 Doppler widths. It is necessary to go to such large values of $x_{\max}$, because for $v_g = 1600\ \mathrm{m\ s^{-1}\ km^{-1}}$ the maximum non-dimensional velocity within the VALC atmosphere is about 1250 Doppler widths. We divide the wavelength grid into three ranges, namely $[-0.4, +0.4]$ Å, $[-10, +10]$ Å (which excludes the first range), and the remaining range up to ± 100 Å

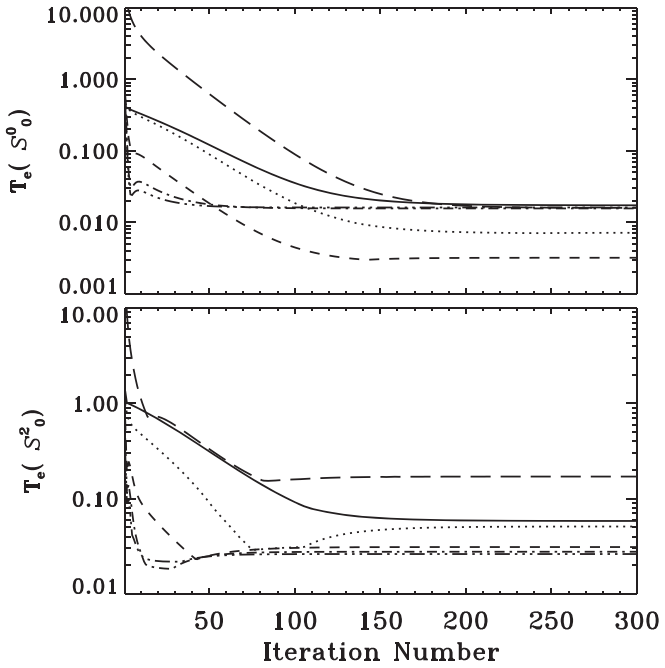

Figure 3. Surface true error of $\mathcal{S}_0^0$ (top panels) and of $\mathcal{S}_0^2$ (bottom panels) computed with the CMF method. The VALC model atmosphere is considered. Different curve types are: static case (solid curve), a linear velocity field with $v_g = 2.23$ m s^{-1} km^{-1} (dotted curve), $v_g = 8.92$ m s^{-1} km^{-1} (dashed curve), $v_g = 15.61$ m s^{-1} km^{-1} (dotted–dashed curve), $v_g = 20.07$ m s^{-1} km^{-1} (dash-triple-dotted curve), and a damped sine wave at $t = 30$ s (long-dashed curve).

(excluding the first two ranges). The first wavelength grid (grid 1 hereafter) has 1019 points with spectral resolution of 0.005 Å in the first range, 0.025 Å in the second range, and 20 Å in the third range. Grid 2 has 401 points, with spectral resolution of 0.005 Å in the first range, and unequal spacing in both the second and third ranges. Grid 3 has 201 points, with 0.01 Å spacing in the first range, and unequal spacing in the remaining ranges. Grid 4 has 149 points, with a spacing of 0.025 Å in the first range, and unequal spacing in the remaining ranges.

We first discuss the strong line case. In Figures 4(a) and (b), we study the behavior of this numerical oscillation with the number of wavelength grid points. This is because the numerical oscillations originate from the frequency discretization of the CMF term (see Equation (6)), which is in disagreement with Hauschildt & Baron (2004). Figure 4(b) is computed using the very fine wavelength grid, namely grid 1. In Figure 4(a), the solid curve is computed using grid 2, dotted curve using grid 3, and dashed curve using grid 4. We obtain numerical oscillations in the case of all four wavelength grids. These oscillations are largest for the finest grid (i.e., grid 1), and reduce when the wavelength grid is more crude. However the solutions from grid 3 and grid 4 nearly coincide (compare the dotted and dashed curves in Figure 4(a)). We have verified that these oscillations continue to exist irrespective of whether we use PRD or CRD for the frequency redistribution. Furthermore, these oscillations remain in the intensity profile, even if we neglect polarization.

Hauschildt & Baron (2004) discuss such numerical instability for the second discretization scheme, which is the one adopted in P1 and in this paper. These authors show that this numerical instability can be overcome using the first discretization scheme of Hauschildt (1992), or a mix of first and second discretization schemes. We have also implemented both the first and mixed discretization schemes of Hauschildt & Baron (2004) in our CMF code. However, we continue to obtain numerical oscillations similar to those shown in Figures 4(a) and (b) for both the first and mixed discretization schemes. Unlike the second and mixed discretization schemes, the first discretization scheme converges rather slowly as in this case the effect of the CMF term is not included in the approximate lambda operator (see Hauschildt 1992).

We now turn our attention to the weaker line case. In Figure 4(c), the solid black curve is computed using grid 1 and the dashed red curve with grid 3. Clearly, the numerical oscillations are non-existent for grid 3, while some oscillations are seen for grid 1 but with much reduced amplitudes compared to the strong line case.

We remark that for v_g less than 1600 m s^{-1} km^{-1} we do not obtain any numerical oscillations in the converged solution. Such high velocity fields are of relevance only to supernova atmospheres. For solar- or stellar-type velocity fields (also including those in stellar winds), the CMF methods presented here and in P1 have been tested and found to be accurate.

6. STOKES PROFILES FORMED IN A NON-MAGNETIC MOVING ATMOSPHERE

Figures 5 and 6 display the time evolution of the emergent Q/I profiles at $\mu = 0.1$ and $\mu = 0.9$ respectively. Although the linear polarization produced due to non-magnetic scattering is highly reduced near the disk center ($\mu = 0.9$) due to the limb brightening effect, the effect of the vertical velocity fields are felt largest there. Therefore in Figure 6 we present the emergent profiles for $\mu = 0.9$, to illustrate the effect of velocity fields. The vertical velocity wave given by Equation (9) and shown in Figure 1 is used for the computations. In the bottom Q/I panels of Figures 5 and 6 the solution from a static atmosphere is shown as a dotted curve. In Figure 5, we also present the radiation anisotropy ($\bar{J}^2_0/\bar{J}^0_0$) for different wavelengths and at time point $t = 30$ s. We recall that the mean intensity vector is given by the integral term in Equation (4). The $\bar{J}^2_0/\bar{J}^0_0$ for the static case is shown as black curves. Because there exists symmetry about the line center in the static case, the anisotropies for $\pm(\lambda - \lambda_0)$ coincide.

From Figures 5 and 6, we see that all the expected dependences of the Q/I and the radiation anisotropy on the vertical velocity gradients are correctly reproduced by our CMF code in the limit of PRD. These include Doppler shifts, asymmetries around the line center, and dependence of Q/I on the anisotropy, namely enhancement of anisotropy in the higher layers (compare the green and black solid curves in the left panel of Figure 5) leading to enhancement in Q/I around the line core region (compare for example the solid and dotted curves in the bottom Q/I panels of Figures 5 and 6). Since these known effects of the vertical velocity gradient are discussed in detail in Carlin et al. (2012, see also P1) we do not elaborate further on them.

The effect of wave motion can be seen in the temporal fluctuation of the Doppler shifts and Q/I amplitudes (see the top Q/I panels of Figures 5 and 6) as already discussed in Carlin et al. (2013). In particular the distortions in profile shape produced by the velocity wave are significant for $\mu = 0.9$ (see the bottom Q/I panel of Figure 6), which seem to propagate in wavelength space with an increase in time within a wave period (see the top Q/I panel of Figure 6). The wave motion gives rise to wavy patterns in the radiation anisotropy, which are mainly

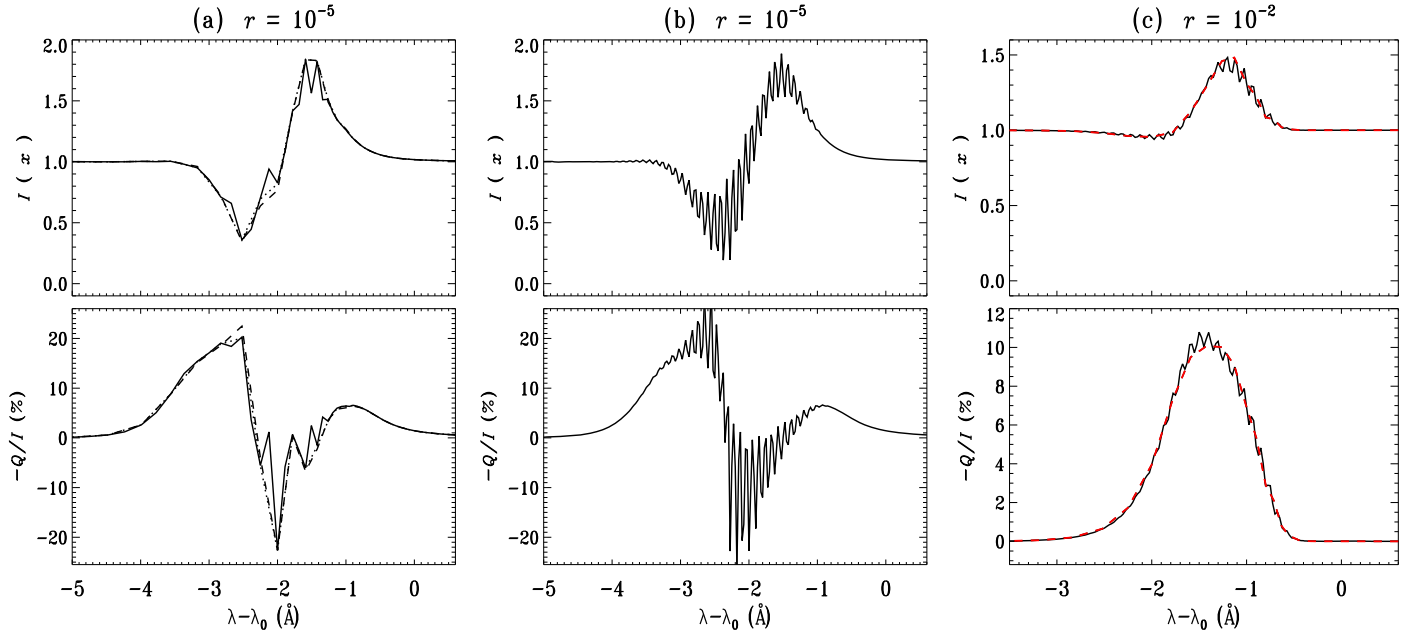

Figure 4. Numerical instability of the CMF method for very large velocity fields. The VALC model atmosphere with a linear velocity field having a constant velocity gradient $v_g = 1600$ m s^{-1} km^{-1} is used for the computation. Emergent intensity and linear polarization profiles at a line of sight of $\mu = 0.1$ are shown. Panels (a) and (b) correspond to a strong line with $r = 10^{-5}$, and panel (c) corresponds to a weaker line with $r = 10^{-2}$. See Section 5.3 for details.

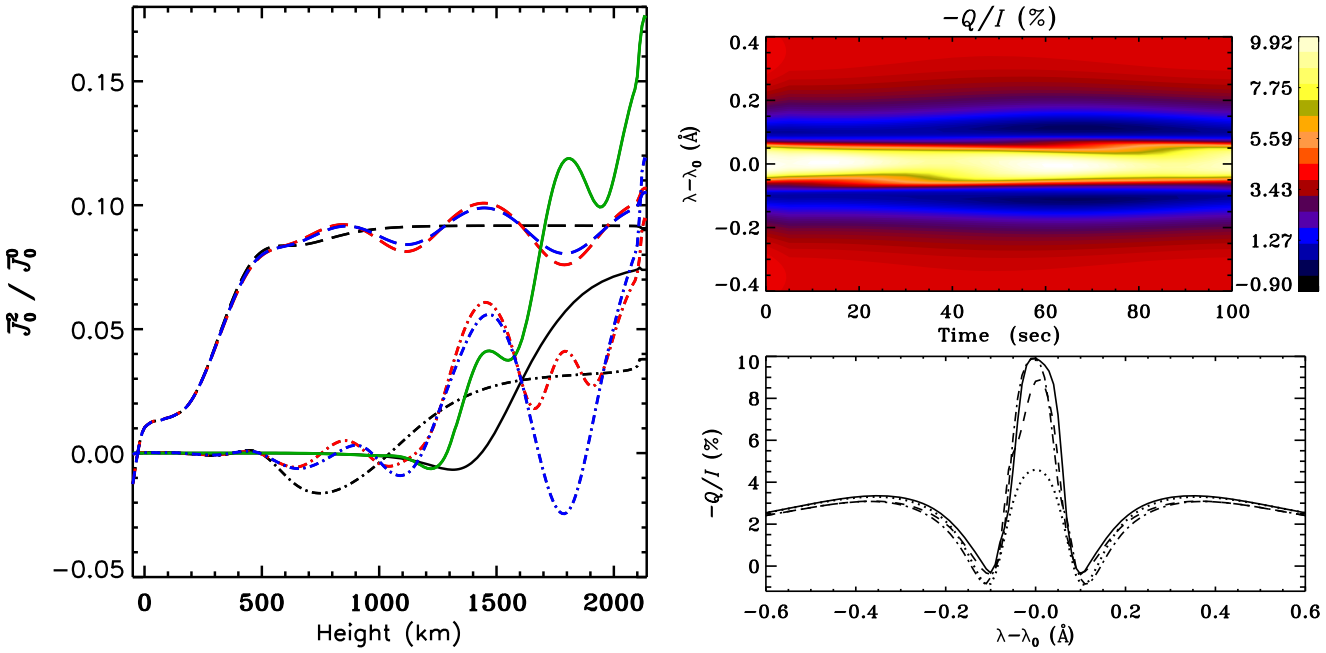

Figure 5. The left panel shows the radiation anisotropy ($\bar{J}^2_0/\bar{J}^0_0$) vs. height in the VALC model atmosphere for the static case (black curves) and for a damped sine wave at time point $t = 30$ s (colored curves). The solid curves correspond to the line center, dotted–dashed curves to the blue and red side core minima, and the dashed curves to the blue and red side PRD wing peaks. For the static case the anisotropy corresponding to the blue and red side wavelength points coincide and are shown with black curves, while in the velocity wave case they differ and are distinguished by blue and red curves. The top right panel shows the time evolution of the emergent Q/I profiles at a line of sight of $\mu = 0.1$. The bottom right panel shows the corresponding line profiles for $t = 0$ s (solid curve), $t = 30$ s (dashed curve), and $t = 60$ s (dotted–dashed curve). The solution computed in a static atmosphere is shown as dotted curve for comparison. The vertical velocity wave used for the computation is shown in Figure 1.

seen in the higher layers for line center wavelength and also in the somewhat deeper layers for wavelengths away from the line center (see the colored curves in the left panel of Figure 5).

In the case of PRD, the presence of a velocity gradient in the line-forming region can give rise to asymmetric core minima (namely, minima between the core peak and the wing PRD peaks) and wing PRD peaks. This effect, discussed in detail in P1, is, however, independent of the non-monotonicity of the velocity field. In the case of a damped sine wave, we see only a marginal asymmetry in the blue and red core minima for $\mu = 0.1$, while the wing PRD peaks are nearly symmetric about the line center. This can be understood by comparing the values

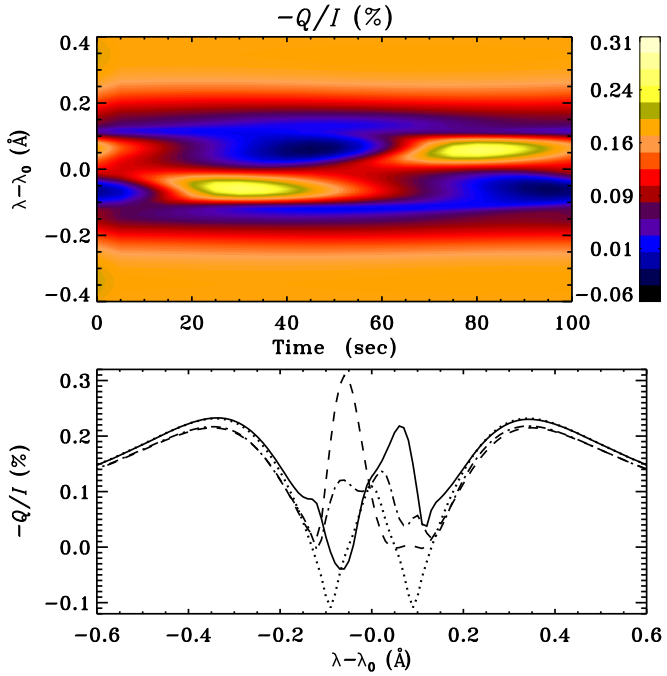

Figure 6. Time evolution of Q/I profiles formed in a VALC model atmosphere at $\mu = 0.9$. Different curve types in the bottom panel have the same meaning as in the bottom right panel of Figure 5.

Table 2
Height Corresponding to $\tau_{x\mu} = 1$ for Line Center, Core Minima, and PRD Wing Peaks for a Line of Sight of $\mu = 0.1$

$(\lambda - \lambda_0)$ in Å	Height in km at which $\tau_{x\mu} = 1$	
	Static	Damped sine Wave ($t = 30$ s)
−0.36 (blue PRD peak)	450	450
−0.11 (blue core minimum)	690	720
0 (line center)	1680	1680
0.11 (red core minimum)	690	675
0.36 (red PRD peak)	450	450

of radiation anisotropy between the blue and red wing PRD peaks at the height where these peaks are formed. In Table 2 we give the height at which the total monochromatic optical depth for a given $(\lambda - \lambda_0)$ (or x) and μ (denoted here as $\tau_{x\mu}$ and defined below Equation (1)) is equal to unity for the static case and for the damped sine wave at $t = 30$ s. We have chosen the values of $(\lambda - \lambda_0)$ for the line center, blue and red core minima, and blue and red PRD wing peaks keeping the static case as the reference, although these values are different in the presence of a velocity wave due to Doppler shift. However, for $\mu = 0.1$ and $t = 30$ s, this difference is minimal. From Table 2 we see that the wing PRD peaks are formed at a height of 450 km for both the static and damped sine wave. At this height the anisotropies for the blue and red wing PRD peaks nearly coincide (compare the blue and red dashed curves in the left panel of Figure 5), thereby leading to the wing PRD peaks that are nearly symmetric about the line center (see the bottom Q/I panel in Figure 5).

Figure 7 shows the response of the Stokes profiles at $t = 10$ s to the variations in propagation speed c_p of the velocity wave. The period of the wave is held constant at $P = 100$ s. Therefore as c_p increases, the wavelength of the

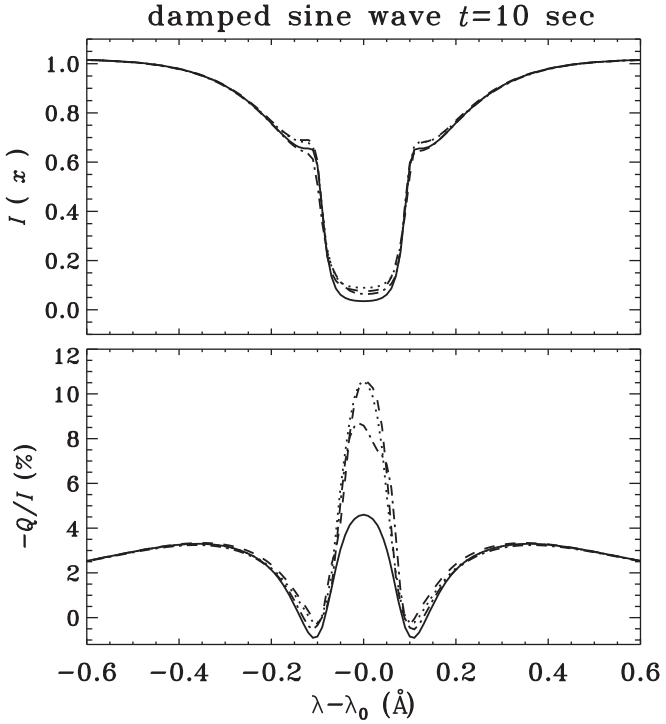

Figure 7. Effect of propagation speed c_p on the Stokes profiles for a nearly horizontal ray $\mu = 0.1$. The emergent $(I, Q/I)$ profiles computed with a damped sine wave at the time point $t = 10$ s are shown. Different curves are: static case (solid curve), $c_p = 3$ km s^{-1} (dotted curve), $c_p = 7$ km s^{-1} (dashed curve), and $c_p = 11$ km s^{-1} (dotted–dashed curve).

wave $\lambda_w = c_p P$ also increases. In other words, the number of wavelengths or waves that cover the entire atmosphere decreases. We remark that the resolution of the height grid is 15 km, while the shortest wavelength considered is 300 km. Therefore the spatial grid is sufficiently fine to correctly handle the case of a large number of waves within the atmosphere. Indeed we have verified that the emergent profiles presented in Figure 7 coincide with those computed with a height grid of 5 km resolution. In the case of $c_p = 3$ km s^{-1}, wherein there are large numbers of waves within the atmosphere, the opacity also executes fluctuations more often within the atmosphere. Therefore, the overall anisotropy of the radiation field increases uniformly throughout the atmosphere. This results in a considerable increase in the magnitude of the Q/I profiles in the line core region. The Q/I profiles do not show any systematic variation with c_p. On the other hand the intensity profiles are somewhat insensitive to variations in c_p.

The emergent $(I, Q/I)$ profiles computed using the VALC model atmosphere with the linear velocity field are shown in Figure 8. As the velocity gradient v_g increases the Doppler shift (a blueshift in this case) of the profiles also increases. The linear polarization initially increases and then saturates followed by a small decrease. The increase in Doppler shift is more dramatic for $\mu = 0.9$ than for $\mu = 0.1$. The profiles are asymmetric about the line center. For $\mu = 0.1$ the core minima and the PRD wing peaks exhibit considerable asymmetry about the line center.

We now consider a very strong line $(r = 2 \times 10^{-7})$, representative of the Ca II K line, to demonstrate that our CMF code is able to handle such a difficult case. The other model parameters are the same as those discussed in Section 3. The left panel of Figure 9 shows the response of this very

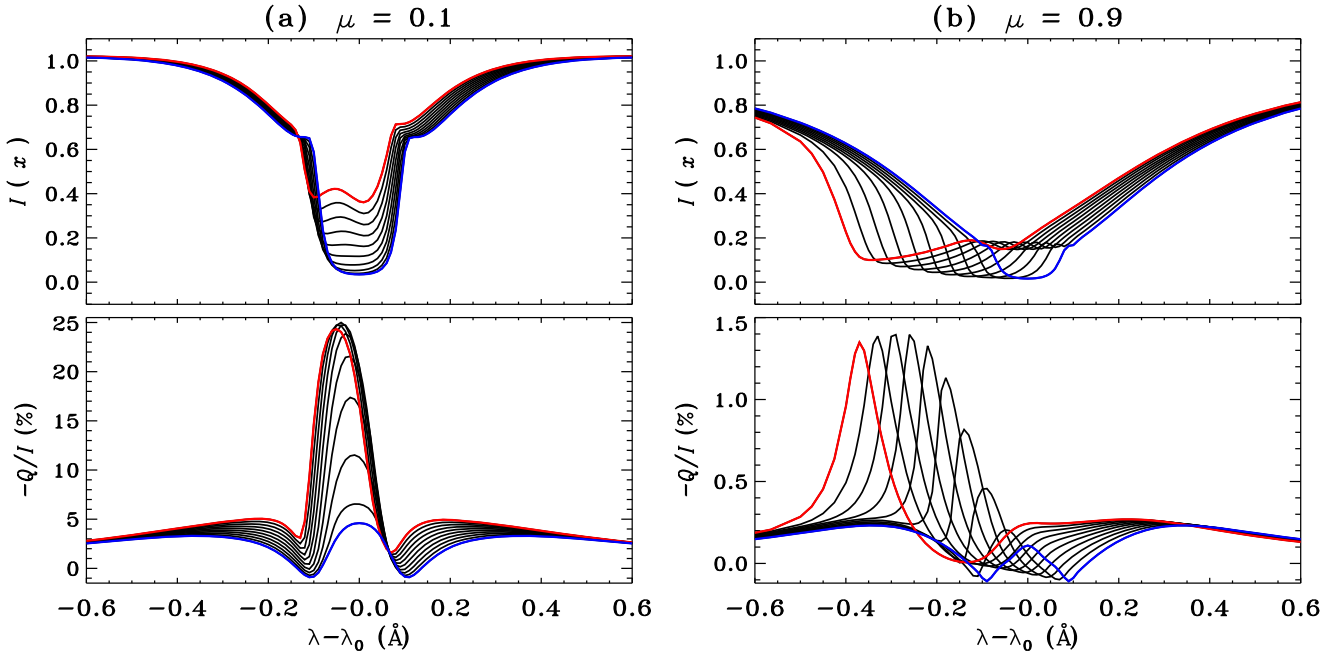

Figure 8. Emergent (I, Q/I) profiles at $\mu = 0.1$ (panel (a)) and $\mu = 0.9$ (panel (b)) formed in the VALC model atmosphere. A linear velocity field with constant velocity gradient v_g is used for the computation. Different solid curves with increasing (I, Q/I) values correspond to different values of velocity gradient v_g starting from 2.23 to 20.07 m s^{-1} km^{-1} (shown as the red curve) in steps of 2.23 m s^{-1} km^{-1}. The solution computed in a static atmosphere is shown as the blue curve for comparison.

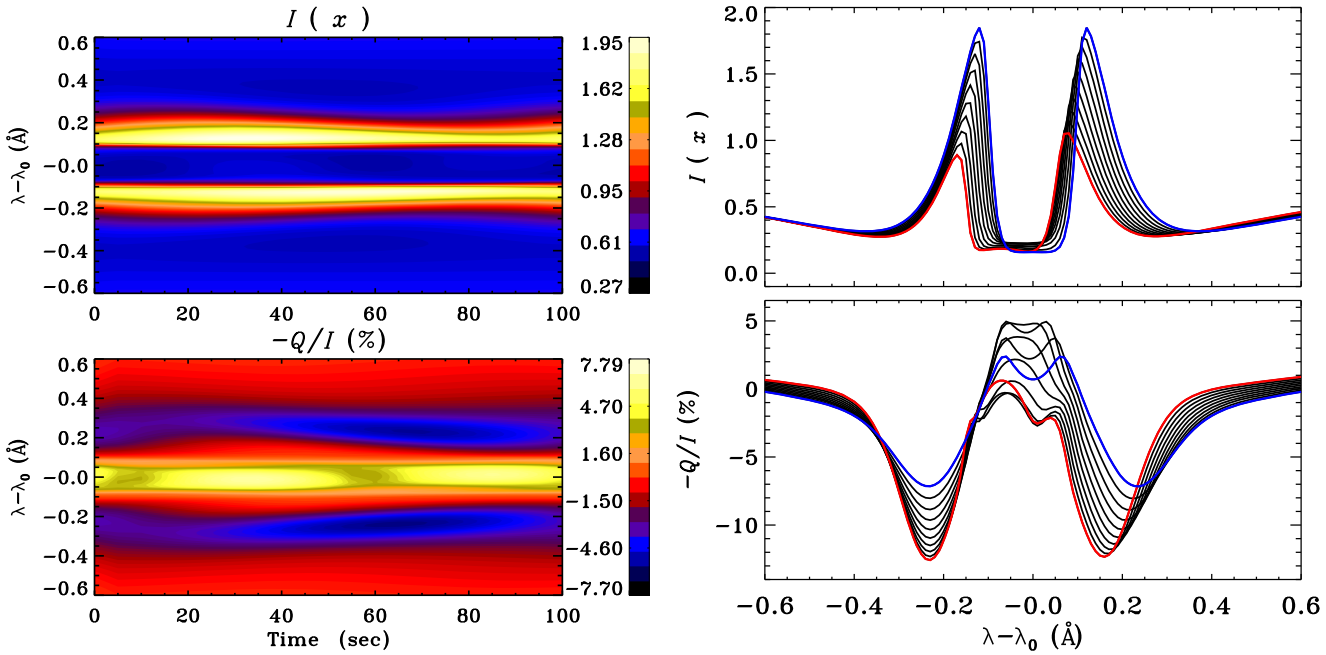

Figure 9. Stokes profiles of a very strong line ($r = 2 \times 10^{-7}$) formed in a VALC model atmosphere for a nearly horizontal ray at $\mu = 0.1$. The left panel shows the time evolution of the emergent (I, Q/I) profiles computed using a damped sine wave. The right panel shows the emergent (I, Q/I) profiles computed using a linear velocity field. Different curve types have the same meaning as in Figure 8(b).

strong line emergent at $\mu = 0.1$ to a damped sine wave. The nature of the intensity profile for such a strong line case has been discussed in Shine et al. (1975) for the static case and by Scharmer (1984) for the velocity wave case. Our CMF code is able to reproduce the expected self-reversed absorption line with symmetric emission peaks on either side of the line center (see the blue curve in the right panel of Figure 9) for the static case, and Doppler shifted asymmetric profiles in the presence of velocity waves. Furthermore, our code is able to reproduce the fluctuation of these emission peaks both in amplitude and in their wavelength position for different time points of the wave, as already noted by Scharmer (1984). As for the corresponding Q/I profiles, a detailed study for the static case is presented in Saliba (1985) and in Stenflo (1980), who discusses the effect of the continuum parameter r. The bottom left panel of Figure 9 shows the effect of the vertical velocity wave on Q/I. Being a

very strong line, this line forms high in the atmosphere, thereby the effect of the velocity field can be felt over a larger wavelength domain within the line.

The right panel of Figure 9 displays the emergent (I, Q/I) profiles for the very strong line case computed using the linear velocity field. As expected, Doppler shifted asymmetric profiles are obtained as the velocity gradient v_g increases. Also, the emission peaks in the intensity profile decrease in amplitude, the decrease being asymmetric and larger for the blue emission peak. Such highly asymmetric intensity profiles were obtained by Scharmer (1984). Apart from the Doppler shift the Q/I profiles exhibit a non-linear variation in their amplitude in and around the line core region.

7. CONCLUSIONS

In this paper we have considered the problem of polarized line formation in planar media where non-relativistic, non-monotonic vertical velocity fields exist. For this purpose, we have suitably modified the CMF method presented in P1 to handle non-monotonic vertical velocity fields. To this end, in P1 and in this paper, we have applied the CMF method of Hauschildt & Baron (2004) with the second discretization scheme for the CMF term to include polarization and PRD.

In the first part of the paper we present several numerical tests to validate the CMF method. We show that the CMF method is sufficiently accurate and can be used for solar and stellar applications. For velocities that prevail in supernova atmospheres the CMF method becomes numerically unstable, producing oscillations in the converged solution, particularly for the case of optically thick lines. Therefore we conclude that the CMF methods presented here and in P1 are reliable for velocity gradients less than $1600\,\mathrm{m\,s^{-1}\,km^{-1}}$. For larger velocity gradients our CMF method should be used with caution, in particular for the strong line case.

In the second part of the paper we present the Stokes profiles emerging from a VALC model atmosphere with (i) a vertical velocity wave represented by a damped sine wave and (ii) a linear velocity field. We show that our CMF code is able to reproduce the expected behavior of emergent Stokes profiles and radiation anisotropy with the variation in velocity gradient (see Carlin et al. 2012, 2013; Sampoorna & Nagendra 2015a, 2015b). As in the previous studies by the above-cited authors, the present study also demonstrates that the linear polarization profiles respond more sensitively to the velocity fields than the intensity profiles. Therefore linear polarization together with intensity provide a better diagnostic tool to explore the nature of velocity fields in the internal layers of solar or stellar atmospheres.

The authors are grateful to an anonymous referee for constructive comments that helped to substantially improve the paper. We would like to thank Dr. L. S. Anusha for her help in making some of the figures presented in this paper. Computations are performed on a 20 node HYDRA cluster (dual Xeon X5675 with 6 cores per processor and 3.06 GHz clock speed), FORNAX (dual opteron 6220 with 8 cores and 3.0 GHz clock speed), and KASPAR (dual Xeon X5675 with 6 cores per processor and 3.06 GHz clock speed) computing facilities at the Indian Institute of Astrophysics. We would like to thank Dr. M. Bianda, IRSOL, Switzerland, for supporting our visit to SPW8 and IRSOL during which some of the revisions were completed.

REFERENCES

Anusha, L. S., Nagendra, K. N., Bianda, M., et al. 2011, ApJ, 737, 95
Anusha, L. S., Nagendra, K. N., Stenflo, J. O., et al. 2010, ApJ, 718, 988
Auer, L., Fabiani Bendicho, P., & Trujillo Bueno, J. 1994, A&A, 292, 599
Baron, E., & Hauschildt, P. H. 2004, A&A, 427, 987
Cannon, C. J. 1973, ApJ, 185, 621
Carlin, E. S., & Asensio Ramos, A. 2015, ApJ, 801, 16
Carlin, E. S., Asensio Ramos, A., & Trujillo Bueno, J. 2013, ApJ, 764, 40
Carlin, E. S., Manso Sainz, R., Asensio Ramos, A., & Trujillo Bueno, J. 2012, ApJ, 751, 5
Faurobert-Scholl, M. 1992, A&A, 258, 521
Fontenla, J. M., Avrett, E. H., & Loeser, R. 1993, ApJ, 406, 319
Fontenla, J. M., Curdt, W., Haberreiter, M., Harder, J., & Tian, H. 2009, ApJ, 707, 482
Frisch, H. 2007, A&A, 476, 665
Hauschildt, P. H. 1992, JQSRT, 47, 433
Hauschildt, P. H., & Baron, E. 2004, A&A, 417, 317
Holzreuter, R., Fluri, D. M., & Stenflo, J. O. 2005, A&A, 434, 713
Hubeny, I., & Mihalas, D. 2014, Theory of Stellar Atmospheres: An Introduction to Astrophysical Non-equilibrium Quantitative Spectroscopic Analysis (Princeton, NJ: Princeton Univ. Press)
Hummer, D. G. 1962, MNRAS, 125, 21
Mihalas, D. 1978, Stellar Atmosphere (2nd edn; San Francisco, CA: Freeman)
Mihalas, D., Kunasz, P. B., & Hummer, D. G. 1975, ApJ, 202, 465
Mihalas, D., Shine, R. A., Kunasz, P. B., & Hummer, D. G. 1976, ApJ, 205, 492
Nagendra, K. N. 1996, SoPh, 164, 67
Noerdlinger, P. D., & Rybicki, G. B. 1974, ApJ, 193, 651
Olson, G. L., & Kunasz, P. B. 1987, JQSRT, 38, 325
Parker, E. N. 2007, Conversations on Electric and Magnetic Fields in the Cosmos (Princeton, NJ: Princeton Univ. Press)
Rangarajan, K. E. 1997, A&A, 320, 265
Rangarajan, K. E. 1999, in Solar Polarization, ed. K. N. Nagendra & J. O. Stenflo (Dordrecht: Kluwer), 179
Rutten, R. J. 2007, in ASP Conf. Ser. 368, The Physics of Chromoshperic Plasmas, ed. P. Heinzel, I. Dorotovič, & R. J. Rutten (San Francisco, CA: ASP), 27
Saliba, G. J. 1985, SoPh, 98, 1
Sampoorna, M., & Nagendra, K. N. 2015a, in IAUS 305, Polarimetry: From the Sun to Stars and Stellar Environments, ed. K. N. Nagendra et al. (Cambridge: Cambridge Univ. Press), 387
Sampoorna, M., & Nagendra, K. N. 2015b, ApJ, 812, 28 (P1)
Sampoorna, M., Nagendra, K. N., & Frisch, H. 2008, JQSRT, 109, 2349
Scharmer, G. B. 1984, in Methods in Radiative Transfer, ed. W. Kalkofen (Cambridge: Cambridge Univ. Press), 173
Shine, R. A., Milkey, R. W., & Mihalas, D. 1975, ApJ, 201, 222
Smitha, H. N., Nagendra, K. N., Stenflo, J. O., et al. 2015, in IAUS 305, Polarimetry: From the Sun to Stars and Stellar Environments, ed. K. N. Nagendra et al. (Cambridge: Cambridge Univ. Press), 372
Stenflo, J. O. 1980, A&A, 84, 68
Supriya, H. D., Smitha, H. N., Nagendra, K. N., et al. 2014, ApJ, 793, 42
Taroyan, Y., & Erdélyi, R. 2009, SSRv, 149, 229
Vernazza, J. E., Avrett, E. H., & Loeser, R. 1981, ApJS, 45, 635